Publication Year	2021
Acceptance in OA	2025-03-13T15:09:20Z
Title	Reconnection nanojets in the solar corona
Authors	Antolin, Patrick, PAGANO, Paolo, Testa, Paola, PETRALIA, Antonino, REALE, Fabio
Publisher's version (DOI)	10.1038/s41550-020-1199-8
Handle	http://hdl.handle.net/20.500.12386/36762
Journal	NATURE ASTRONOMY
Volume	5

Reconnection Microjets in the Solar Corona

Patrick Antolin[1,*], Paolo Pagano[1], Paola Testa[2], Antonino Petralia[3], Fabio Reale[3,4]

[1]*School of Mathematics and Statistics, University of St. Andrews, St. Andrews, Fife KY16 9SS, UK*

[2]*Harvard-Smithsonian Center for Astrophysics, 60 Garden St., Cambridge, MA 02138, USA*

[3]*INAF-Osservatorio Astronomico di Palermo, Piazza del Parlamento 1, 90134, Palermo, Italy*

[4]*Dipartimento di Fisica & Chimica, Università di Palermo, Piazza del Parlamento 1, 90134, Palermo, Italy*

Coordinated observations with the Atmospheric Imaging Assembly (AIA) of the *Solar Dynamics Observatory* (*SDO*), the *Interface Region Imaging Spectrograph* (*IRIS*) and the Solar Optical Telescope (SOT) of *Hinode* were combined with state-of-the-art numerical simulations to reveal the direct observational signature of a nanoflare produced by magnetic reconnection in the solar corona. A swarm of these elemental heating events is observed with unprecedented detail, leading to the coronal heating of a loop structure. The loop is initially subject to thermal instability leading to the appearance of coronal rain that allows the dynamic and minute tracing of the coronal magnetic field during the reconnection process and heating to multi-million degree temperatures. Single and clustered reconnection events can be distinguished and are characterised by a strong transverse displacement of an internal loop strand, a localised intensity burst in the strand and, in particular, the presence of a microjet – a fast (≈ 200 km s^{-1}), bursty, very short lived (on the order of 10 s or less)

and small-scale (500 km width, 1500 km in length) jet-like structure stemming from the rain strand and perpendicular to it, accelerated by magnetic tension (slingshot effect) during the magnetic reconnection process at small angles. The strongest events are accompanied by the ejection of small-scale plasmoids along the jet axis, perpendicular to the loop. The observed microjets have an estimated energy of the order of 10^{25} erg. The spatial and temporal evolution of the reconnection events show characteristics of a magnetohydrodynamic (MHD) avalanche: the events are first clustered and highly localised near the loop apex. They expand within minutes across and along the loop. Bi-directional flows along the loop, internal rotational motions, a decrease in the amount of braiding of the loop and an increase in the overall loop intensity accompany the entire process. Supported by our numerical simulations, these localised, telltale observational signatures of magnetic reconnection that we attribute to the elemental nanoflares allow to clearly differentiate reconnection-driven heating mechanisms with the coronal heating candidates for which reconnection does not play a central role.

One of the most puzzling unsolved problems in astrophysics is in the Earth's backyard: the solar corona. This outer layer of the Sun's atmosphere is characterised by plasma at multi-million degree temperatures, hundreds of times higher than the underlying photosphere, the Sun's surface. Magnetic reconnection is a major candidate to heat and maintain the solar corona [1]. This mechanism relies on quasi-steady, slow stress of the coronal magnetic field to produce twisted and braided structures: non-potential magnetic field topologies with free energy that can be impulsively released through magnetic reconnection. Misaligned magnetic field lines are brought together along quasi-separatrix surfaces, producing current sheets in which the plasma is heated through Ohmic and viscous dissipation. Numerical simulations suggest that at the reconnection point plasmoid structures are formed through the secondary tearing instability, they merge and are ejected with the reconnection outflow (also known as reconnection jets), accelerated by the release of magnetic tension to Alfvénic speeds [2, 3, 4]. These processes have been observed in large-scale current sheets during solar flares [5, 6, 7] or in low-lying chromospheric structures [8].

Observations of cold and dense material in the solar corona, such as prominences and coronal rain, offer more direct observations of processes related to reconnection [9, 10]. Indeed, a higher resolution is achieved when observing in visible wavelengths associated with cool emission. Also the higher optical thickness decreases the line-of-sight confusion. Still, the observations of cold material so far have been restricted to large-scale changes in the magnetic field following reconnection, large plasmoids in long current sheets, or plasma outflow at Alfvénic speeds along the reconnected magnetic field.

Parker pioneered in the reconnection scenario and proposed that coronal loops, the building blocks of the solar corona, undergo myriad of tiny reconnection processes in the small misalignments of the braided field lines, each releasing a small amount of energy that is rapidly redistributed by thermal conduction along the reconnected field [11]. These tiny outbursts of energy lead to nanoflares – impulsive intensity bursts on the order of 10^{24} erg – and a loop is thought to be heated by a nanoflare storm [12, 13]. So far, studies revealing the existence of nanoflares and their link to the heating of the solar corona have been indirect, based on the presence of very high temperatures of 10 million degrees in the non-flaring solar corona [14]. High temperatures have been considered to be the smoking gun of nanoflares in reconnection-based heating models since they have not been reproduced by other heating models not based on reconnection, such as wave heating. However, absence of evidence is not evidence of absence. Furthermore, wave heating models have also been able to reproduce nanoflares as single bursts of intensity [15, 16]. It is still unclear whether reconnection-based nanoflares can be discriminated and whether single nanoflares could indeed be observed as separate and countable events, as suggested by theory.

A requirement to achieve coronal heating by a nanoflare storm due to reconnection is that it is triggered by a switch-on mechanism that acts only when the stressed field holds enough free energy to heat the loop. A popular theory for the switch-on mechanism is the MHD avalanche model: the system reaches a critical state in which the local loss of equilibrium within elemental loop structure (strands) leads to the destabilisation of the entire structure, producing a nanoflare storm that heats the entire coronal loop [17, 18, 19]. How this critical state is reached is another conundrum in reconnection theory, and a leading mechanism supported by numerical simulations is the kink instability of local strands [20]. This theory suggests that local strands are continuously twisted until one becomes kink unstable and triggers a series of reconnection events that release the free energy of neighbouring strands, not having necessarily reached the critical threshold themselves.

In this work we report the discovery of a reconnection-based nanoflare telltale signature: small-scale microjets that accompany the reconnection process for coronal heating of a loop to multi-million degree temperatures. The spatial and temporal evolution of the heating events and the dynamics of the braided loop structure bear characteristics that can be attributed to an MHD avalanche.

Hinode, *IRIS* and *AIA* co-observed a coronal loop at the limb of the Sun on April 3rd, 2014. Previous to the observation the loop presented a dip at the apex, in which hot material accumulated and catastrophically cooled via thermal instability to form a high standing prominence at a height of $20,000$ km to $40,000$ km (see Figs. 1 and Supplementary Fig.1). From the top of the structure the material flowed as coronal rain along curved paths to the solar surface continuously during several hours. Several rain strands can be observed, and particularly in the 2796 and 1400 SJI filters of *IRIS*, indicating temperatures from $10,000$ K to $100,000$ K [21]. Small apparent misalignments between strands in the plane-of-the-sky (POS) can be seen with maximum angles of $25^\circ \pm 5^\circ$. The EUV absorption from the rain suggests densities of $3.2\times10^{10} - 3.2\times10^{11}$ cm^{-3} (Methods, see also Supplementary Fig. 2). Additionally, upflows were also observed, mainly in the hotter 1400 SJI filter, suggesting constant reloading of material into the prominence from heating events towards the footpoints of the loop. The loop structure was also dimly visible throughout the observation in the EUV 171 channel of *AIA*, indicating mild heating to $700,000$ K degree temperatures.

The focus of this work is on the last 30 min of observation. The loop started an accelerated and differential expansion up to 15 km s^{-1}, with the apex moving outwards while the visible footpoint remained mostly static (see Supplementary material). Almost simultaneous with the expansion, small and localised intensity bursts are first observed at the apparent location of intersection between 2 rain strands near the apex of the loop. The bursts are accompanied by jet-like structure perpendicular to the rain strands with speeds of a few hundred km s^{-1} in the POS, followed by rapid outward transverse displacements and rotational motions up to 60 km s^{-1} of the strands (Figs. 2 and 3). The off-limb observation presents a dark background to the loop structure and a sideways line-of-sight (LOS) to the loop plane. This preferential configuration has allowed a clear distinction of the microjets features. The jets are best visible in the transition region SJI 1400 channel and almost absent in the chromospheric SJI 2796 channel. They have widths on the order of 500 km, lengths of $1,000$ km$-2,000$ km and are extremely short lived (< 10 s). Most are only visible for one snapshot in each instrument, thus indicating POS speeds of 100 km s^{-1}$-$200 km s^{-1}. The first set of microjets is highly clustered at the lower part of the loop near the apex, some separated by $1''$ or less (right column of Fig. 3), lasts about 100 s and brings the largest morphological change within the loop. Other microjets appear isolated (left column of Fig. 3). Most microjets involve strong intensity bursts across all wavelengths (Fig. 4, see also Supplementary material), strand displacements and, for the largest ones, plasmoids ejected along the jets' axis with widths on the order of $1''$ at speeds in the POS of 50 km s^{-1} $-$ 60 km s^{-1} (Fig. 3). Some microjets were captured by the spectrograph of *IRIS* and show a LOS velocity component in the Mg II and Si IV lines above 100 km s^{-1} with a spectral line broadening due to unresolved velocities (i.e. non-thermal) of similar magnitude and an order of magnitude increase in the Si IV line intensity with respect to the average (Figure 4 and Supplementary Fig. 3). We note that the determination of multiple components in the line profiles is relatively straight forward thanks to the off-limb viewpoint and to the low optical thickness of the emission (see Methods). The occurrence of the jets increases with time, together with the intensity of the entire loop in transition region and coronal lines. As the loop expands outwards it also becomes thinner in all channels, with the inner and lower part at the apex showing an apparent and faster outward expansion (Supplementary material). The jets are first concentrated in the inner and lower part of the loop near the apex. In time they rapidly spread out outwards across and along the loop, with some occurring just above spicular heights. The outward trend in the occurrence of the events within the loop matches the rate of the apparent outward expansion and thinning, suggesting magnetic field redistribution within the loop. The temporal and spatial evolution of the microjets and intensity bursts is thus highly suggestive of an MHD avalanche.

Following the expansion, the general brightening of the loop is accompanied by internal rotational motions of the strands at speeds of 50 km s^{-1}, counter-streaming flows along the loop of up to 60 km s^{-1} and non-thermal line broadening of similar magnitude (Supplementary Figs. 4 and 5). The strands from where the jets are rooted become clumpier during their occurrence, suggesting turbulent flows. A differential emission measure (DEM) analysis of the loop with the AIA channels indicates temperatures of $2 - 5$ MK, with maxima of 10 MK albeit very localised along the loop and therefore less certain (Supplementary Fig. 6b). The observed morphology, dynamics and intensity bursts strongly suggest the presence of braiding, the reduction in time of this quantity with a decrease in the misalignment of the rain strands, and a conversion of magnetic to kinetic and thermal energy during the reconnection process. The dissipated energy is estimated on the order of 10^{25} erg, although this is likely the higher energy end in the occurrence distribution of microjets, the bulk being out of reach for the present instrumentation.

The dynamics of the loop seem strongly linked to the evolution of the prominence at the loop apex. Indeed, the flows downward from the apex start horizontal but gradually become inclined with time, indicating a more pronounced dip of the magnetic field at the apex and therefore an increase in the magnetic stress. Simultaneous to the loop's sudden outward expansion, parts of the prominence are seen to fall vertically towards the surface (Supplementary Fig. 2a), suggesting slipping of the material across the magnetic field either because of its neutrality or due to reconnection from increased downward bending of the dip. The latter is supported by numerical [22] and analytical work [23] on funnel prominences and is shown to lead to the formation of a flux rope. Either way, these scenarios provide a possible explanation for the driver behind the reconnection events. As the prominence weight increases the stress in the field increases. The magnetic field lines freed from the heavy material would rapidly expand outwards from magnetic tension, which would lead to small misalignment and subsequent reconnection with the lower field lines still anchored to the prominence above (see sketch in Supplementary Fig. 7). This scenario can explain the observed localised features such as the brightening, the microjet, the plasmoids and the strand displacement.

To confirm that microjets with the observed characteristics are indeed possible through reconnection at small-angle misalignments between rain strands and to further examine their nature we conduct a 3D MHD experiment of 2 slightly misaligned flux tubes reconnecting at one point in the corona (Methods). A highly localised reconnection event is obtained which satisfactorily explains the microjet as one of the bi-directional reconnection outflows and field line displacement accelerated by magnetic tension (Figure 5). Crucially, this type of small angle reconnection does not involve a strong plasma flow along the reconnected field lines. The strongest dynamics (and the microjets) come from the perpendicular advection of the field lines from the reconnection site, with relatively small longitudinal plasma velocity. Besides the overall shape and the dynamics, we also recover the local temperature increase and the larger-scale perpendicular displacement of the reconnecting field lines (that would characterise a strand in the presence of rain).

On the global scale, the appearance of the prominence and the rain, the formation of a flux rope and the transfer of twist is well explained by the funnel prominence model. Although not proven in [22] due to the 2.5D MHD limitation, the model also conjectures the loss of stability and eruption of the structure due to the kink instability. This is also suggested by our AIA observations, which show that after the co-observation period the loop disappears and the entire structure collapses downwards first before being ejected laterally producing a partial eruption and the formation of a very high loop with twist. We thus conjecture that the loss of stability of the prominence if a flux rope is present can explain the overall spatial and temporal trend suggestive of an MHD avalanche, including the differential expansion with bottom to top trend from possible magnetic field redistribution and thinning of the loop. The twist composing the flux rope is expected to be partially transferred through reconnection to the loop above, which would explain the strong and rapidly evolving twist within the expanding loop. Despite all these positive matches with the funnel prominence model it is also possible that other scenarios can explain the observed driver and subsequent dynamics.

The combination of microjets, localised intensity bursts and rapid displacement of strands is not only observed during the loop expansion. Much prior to this, two other episodes of clustered microjets are observed, one in a different loop that may not be attached to the prominence (Supplementary material). These episodes involve the same combination of features. These events are isolated in the sense that they only involve a handful of reconnection events and no major morphology change, suggesting a different driver from our main event. Their occurrence suggest that the observed reconnection characteristics occur over various scales and degrees of magnetic field stress, providing a viable path for coronal heating.

The heating events, the detailed dynamics and morphology, and particularly the details of the microjets constitute major challenges for reconnection-based numerical models and provide major constraints on the nature of reconnection in the solar corona. In particular, a major finding from these observations is the discrete and very distinct occurrence of the microjets that, although numerous, appears as a countable phenomenon. This discrete nature may suggest that reconnection occurs episodically and strongly supports the reconnection-based nanoflare theory in that nanoflares constitute elemental heating events that can be responsible for coronal heating. If field lines were continuously reconnecting along current sheets with significant lengths the microjets would not be highly localised but would involve entire rain strands moving perpendicularly at Alfvénic speeds, which is not observed. Furthermore, this process would lead to a smearing of large parts of the displaced rain strands in the *IRIS* images due to the relatively long exposure, which is also not observed. Another possibility is that the rain plays an important role in the reconnection process. The partial ionisation state of the plasma in rain clumps brings the resistivity higher, facilitating reconnection. In this scenario rain clumps would be the preferential locations for reconnection to take place, thereby explaining why the microjets are seen always rooted to rain clumps. Since the rain is observed to be clumpy at high resolution [24] this clumpy character could translate into episodic reconnection. However, as our 3D MHD numerical experiment suggests, highly localised reconnection would happen even in the absence of partially ionised and clumpy plasma. This suggests that the rain is only a catalyst of the process but not a requirement.

Another challenge is the appearance of plasmoids accompanying the microjets at large enough scales to be visible with present instrumentation, suggesting that the magnetic islands involved in the secondary tearing mode instability can grow in non-flare related and small-scale current sheets. We therefore expect that the present microjets constitute the high end of the currently observable spatial and energy scales in this reconnection scenario, and that the bulk of the distribution has energies below 10^{25} erg, as predicted from theory [11]. We can therefore safely predict that next-generation instrumentation will readily observe the distribution of scales of these events. Their distinct observational signatures serve as a base that allows to distinguish heating mechanisms based on magnetic reconnection, thus providing a clear target and path for next-generation high-resolution instrumentation to solve the coronal heating problem.

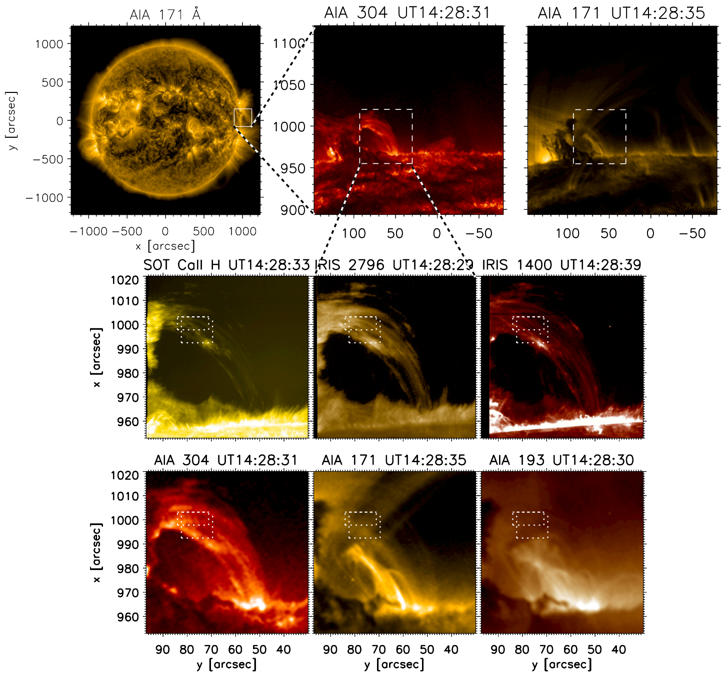

Figure 1: ***SDO, IRIS* and *Hinode* co-observation of a prominence/coronal rain complex at the West limb of the Sun on April 3rd, 2014**. Top-left: full-disk *SDO*/AIA image in the 171 channel. The top two right panels show a zoomed and rotated portion of the FOV (white square) in the AIA 304 and 171 channels. The *IRIS*/SJI FOV is indicated by the white dashed square. Middle 3-panels: Co-observed FOV between *Hinode*/SOT (left, in the Ca II H line) and *IRIS*/SJI (right, in the 2796 and 1400 channels, respectively). A radial filter has been applied to decrease the intensity of the solar disk and to make the off-limb features more visible. Bottom: the corresponding AIA images for the *Hinode* and *IRIS* FOV in the 304, 171 and 193 channels, respectively from left to right. The high-standing prominence core (bright structure to the left in the SOT FOV) is seen as a dark feature in the AIA channels due to Extreme Ultra-Violet (EUV) absorption. The main structure of interest is the loop connecting the prominence to the solar surface. The cool material seen along this loop corresponds to coronal rain. The 2 dotted rectangles within the bottom panels correspond to the FOV of Fig. 2.

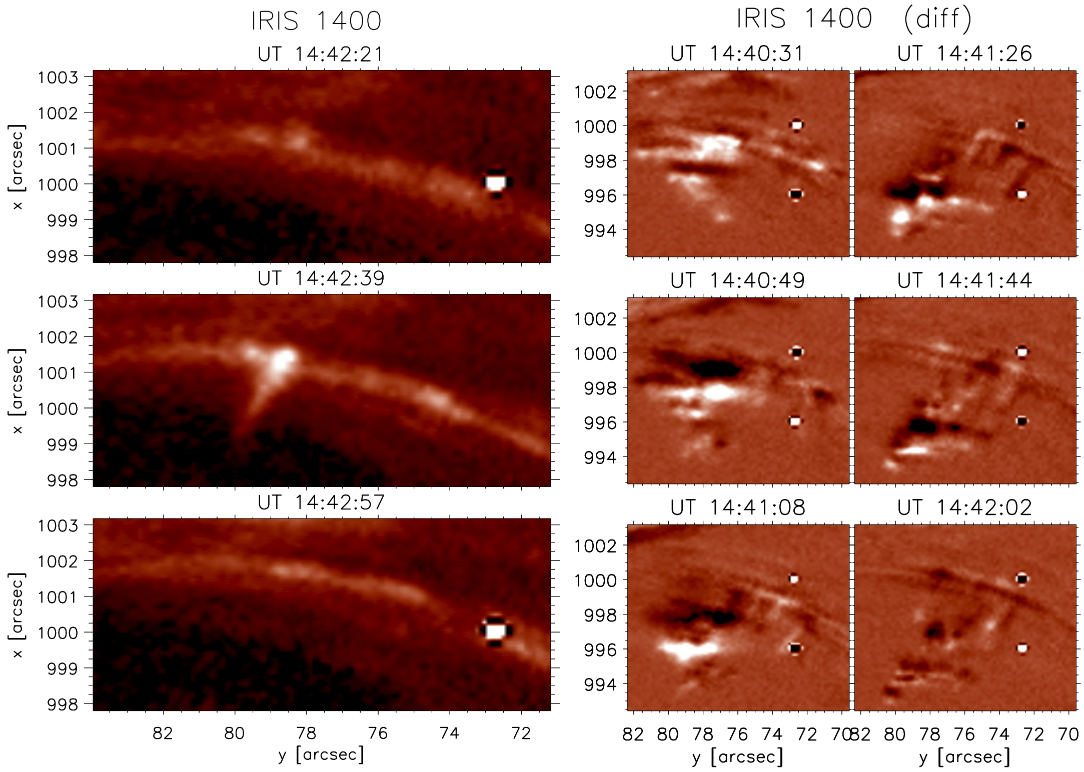

Figure 2: **A single (left) and a cluster (right) of microjets**. From top to bottom (and top left to bottom right for right column) we show consecutive snapshots (18.27 s apart) in the *IRIS*/SJI 1400 channel (in running difference mode for the right set of panels). Both regions capture a small part of the loop seen in Fig. 1 (dotted rectangles in that figure). The single microjet is composed of a bright head stemming from a rain strand, a length of $2'' - 3''$ and an average width of 500 km. Note that this microjet is only seen during one snapshot. The alternating bright and dark pixel from one panel to the other in each panel are an artefact produced by the running difference mode on a cosmic ray. The cluster of microjets are tightly packed, occurring within $1''$ or less from each other. Also, note the ejection of plasmoid-like structure from the cluster. These plasmoids trace new strands that are rapidly separating from the loop after reconnecting.

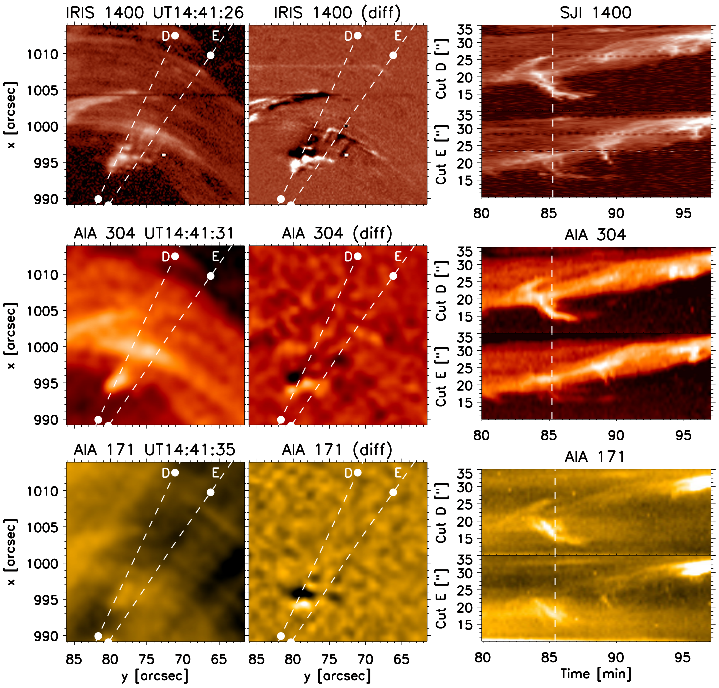

Figure 3: **Plasmoid ejection and perpendicular strand displacement.** From top to bottom the left panels show a pair of a snapshot and its running difference version of a $25'' \times 25''$ portion of the loop in the *IRIS* 1400, AIA 304 and AIA 171 channels, respectively, closest in time to the AIA 304 image. The panels on the right to each image pair shows the time-distance image along cuts D and E (white dashed lines in the images) for the last 19 min of observation and for a distance corresponding to that between the white filled circles along each cut. The moment in time of the images is indicated by the white vertical dashed line in the time-distance image. The cluster of microjets is the same as that shown in Fig. 2. Note that the cluster of microjets and the ejection of plasmoid-like structure along the microjets axis is seen across a wide range of temperatures (see also Supplementary Figs. 7 and 11). The path of the microjets and the plasmoids in the POS is seen as bright downward stretches in the time-distance diagram. An animation of this figure is available online.

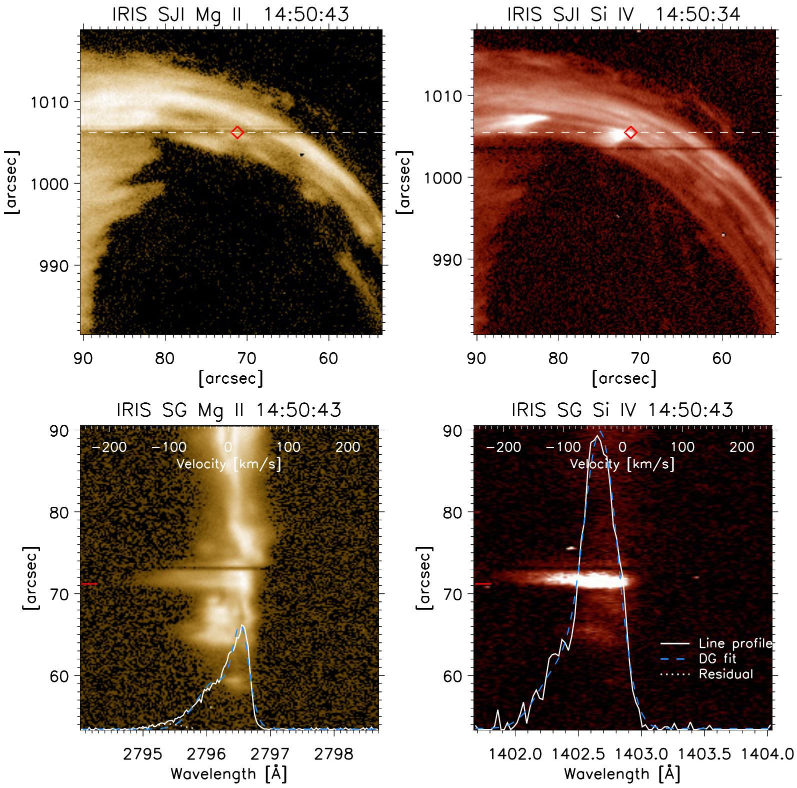

Figure 4: **Spectral features of a microjet.** The top 2 panels show snapshots in the *IRIS*/SJI 2796 (left) and 1400 channels (right) at a time during the apparent expansion of the loop. The location of the *IRIS* slit is shown by the horizontal dashed line. The bottom 2 panels show the spectral profiles in the Mg II k and Si IV 1402.77 Å lines along the slit closest in time to the top images. The small red mark at the slit position of $\approx 71''$ corresponds to the red diamonds in the top images. Overlaid at the bottom are the line profiles (solid white curves), the double Gaussian fit (blue dashed curves) and the residual (white dotted single Gaussian curve) at this location. Note the far blue wing excursion in both lines indicating speeds above 100 km s^{-1} and the strong brightening in the Si IV line, characteristic of a microjet in this loop. The brightening is seen to extend perpendicularly at 2 locations in the SJI images ($\approx 71''$ and $\approx 83''$ indicating 2 microjets).

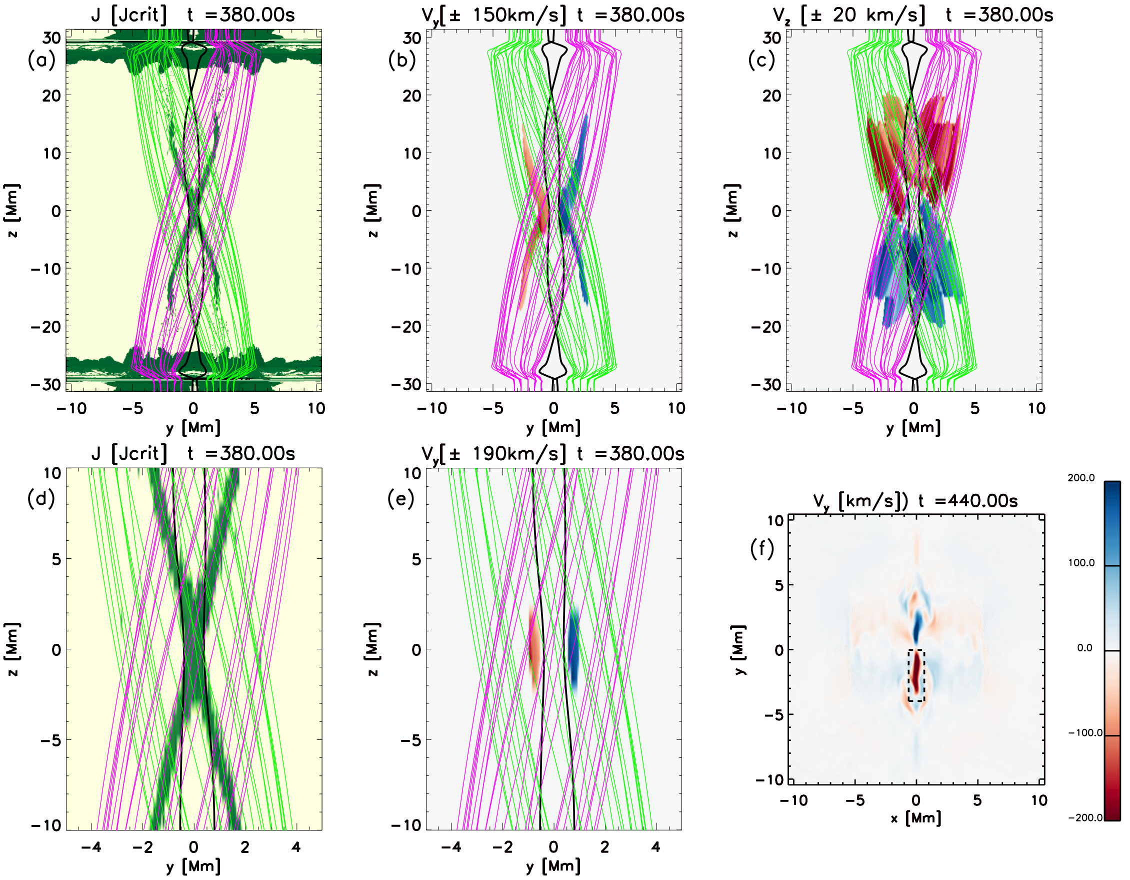

Figure 5: **A microjet in our numerical model.** In all panels, we display magnetic field lines representative of the 2 loops (magenta and green) and reconnected magnetic field lines (black), as described in the Methods section. In the upper row, we show the iso-contour of the electric current where $|J| = J_0$ (a), the iso-contours of the $y-$component of the velocity where $v_y = \pm 150$ km s^{-1} (b) and, the iso-contour of the $z-$compoment of the velocity where $v_z = \pm 20$ km s^{-1} (c). In (d) and (e) we zoom in the central region to show the same contours of the electric currents and where $v_y = \pm 190$ km s^{-1}. In (f) we show the map of the $y-$component of the velocity at $t = 440\ s$ on the plane $z = 0$ that crosses the apex of the two loops. The dashed rectangle represents the $x - y$ dimension of the box over which we compute the energy evolution in Fig. 10.

Methods

Coordinated observations between *Hinode*, *IRIS* and *SDO*. On 2014 April 3, *SDO*, *IRIS* and *Hinode* co-observed a $111'' \times 111''$ field-of-view (FOV) at the West limb of the Sun over active region NOAA 12017 (*IRIS-Hinode* operation plan 254), shown in Fig. 1. Details of this observation are given in [25] and are repeated here for completeness. The *Hinode* Solar Optical Telescope [SOT, 26, 27] observed from 13:16 UT to 14:30 UT in the Ca II H line (formed at a temperature of $20,000$ K approximately), with a cadence of 8 s (1.23 s exposure), with $0''.109$ pixel^{-1} platescale, and an FOV of $111'' \times 111''$, centered at helioprojective coordinates $(x, y) = (996.5'', 31.1'')$. IRIS observed from 13:16 UT to 14:53 UT with a four-step coarse (i.e. with $2''$ steps) raster program (OBS ID 3840259471), with a cadence for the Slit-Jaw Imager (SJI) of 18.27 s (exposure time of 8 s) and 9 s for the spectrograph SG (roughly 37 s per raster position), with $0''.166$ pixel^{-1} platescale ($0''.33$ pixel^{-1} width for the spectrograph), an FOV of $127'' \times 128''$ centered at $(x, y) = (1007.1'', 34.2'')$, containing the SOT FOV. The common FOV to all instruments is shown in Supplementary Fig. 1. The IRIS observing program included both the SJI 2796 and SJI 1400 filtergrams, which are dominated by Mg II k emission at 2796.35 Å around 2×10^4 K and Si iv emission at 1402.77 Å around 10^5 K, respectively. We used 1.5 level data from the Atmospheric Imaging Assembly [AIA, 28], with 12 s cadence and a platescale of $0''.6$ pixel^{-1}.

The SOT data set was processed using the `FG_PREP` Solarsoft routine. The SJI data corresponds to level 2 data [21], which includes correction for thermal variations of the pointing by co-aligning each image using a cross-correlation maximization routine. SOT, SJI, and AIA data were first co-aligned using their respective header information (as provided automatically by the

IRIS website, including solar rotation tracking and roll angles of the *IRIS* instrument). Residual errors in the co-alignment were corrected manually by a cross-correlation process between every 2 channels forming in similar solar conditions.

Geometry of the prominence/coronal rain complex. While only half of the prominence/coronal rain structure can be seen, the observed structure is strongly reminiscent of a funnel prominence as modelled by [22] (see 'Proposed driver' section). The prominence core is high above the ground, it has a tower-like shape and the upper part presents the smallest magnetic dips and is from where most of the coronal rain originates.

IRIS also incorporates a single slit spectrograph (SG), which is placed tangent to the apex of the loop, crossing the prominence. In this observation *IRIS* was performing a large coarse 4-step raster, covering a region of $\approx 5,200$ km in height, across the prominence. The downflow and upflow velocities of the material in the plane of the sky (POS) and along the line-of-sight (LOS) are comparable, and lead to total velocities with a broad distribution peaking at 70 km s^{-1} with the bulk between 30 km s^{-1} and 100 km s^{-1}. The plane of the loop structure is found to be inclined with respect to the LOS with an angle of $55° \pm 5°$ [25]. In this geometry downflows and upflows appear red-shifted and blue-shifted, respectively. The rest wavelength position (i.e. the position corresponding to no flow velocity along the loop) corresponds to a velocity of 16.6 ± 2.3 km s^{-1} with respect to the value in the laboratory, and all velocities presented here have already been accordingly corrected.

Multi-temperature structure and densities. The cool emission from the prominence and leg with coronal rain in Mg II k observed in SJI 2796 and at higher resolution in Ca II H with SOT, and the strong similarity of the structure between SJI 2796 and SJI 1400 (formed at chromospheric and transition region temperatures, respectively) suggests a multi-temperature structure for the material with small dense clumps. Such structure is often observed in coronal rain [29]. We determine the densities through the Extreme Ultra-Violet (EUV) absorption seen in the AIA channels by neutral hydrogen, singly ionised hydrogen and helium (see Supplementary Fig. 2). During the vertical downward motion of the prominence material individual strands can be seen in emission in SJI 1400 and AIA 304 and in absorption in the hotter EUV channels. We select several strands and calculate an average of the absorption features over the time they are observed as single structures. We assume a 5% helium abundance and follow the technique by [30] and [29]. The $L(T)$ function in panels **b** of Supplementary Fig. 2 is defined in [30] and provides the hydrogen column density at the temperature of maximum absorption. Assuming a depth of the strands similar to the width observed in EUV (we take $1,000$ km as a representative value) we can deduce an average for the total hydrogen densities and absorption temperatures where most curves intersect in panel b. We find values of $\log L(T_{abs}) = 18.5 - 19.5$ cm^{-2} for $T_{abs} = 25,000 - 40,000$ K, which correspond to electron densities for the cool absorbing material of $3.2 \times 10^{10} - 3.2 \times 10^{11}$ cm^{-3}.

Spectral line fitting and statistical analysis. The Mg II k and Si IV 1402.77 spectra from the rain changes strongly in time and in space. It usually presents multiple components, broad spectra but also very thin. Contrary to usual on-disk observations for which the Mg II line is optically thick, the optical thickness of this line and, in particular, the presence of a reversed profile at line centre is entirely dependent on the column thickness of the emitting material in the loop along the LOS. Correspondingly, we find a large amount of pixels with Gaussian-like spectral profiles (or with multiple Gaussian components), suggesting optically thin emission. To retrieve the multiple components a multiple Gaussian fitting was performed automatically at every pixel and for every time step. The fitting routine acts based on various thresholds such as large enough signal-to-noise (SNR) ratio, sufficient data points to fit individual profiles and discards pixels hit by cosmic rays. First, a single Gaussian is fitted and the result is used as an initial guess for an additional single and double Gaussian fits. The best fit is selected based on the lowest sigma errors and is then subtracted to the original spectral profile. Additional single Gaussian fits are performed on the residuals on the blue and red parts of the spectra to detect higher Doppler shifted components with high enough SNR that are not captured by the first fits. In this way a maximum of 4 possible components are allowed for each spectral profile. A check on the fitting routine was done based on an extensive visual inspection on random locations in time and space. A total of almost $150,000$ fits were obtained for the Mg II line with a third found to be best represented by a single Gaussian with no other component. The rest was best represented with either a double Gaussian and/or a single Gaussian with additional Doppler components on the blue or red side of the spectrum. The Si IV spectra present in general a much lower SNR, leading to far fewer detections ($10,000$). An additional check on the consistency of the results was then preformed by spatially binning along the slit by 3 pixels and remaking the analysis.

Special care was given to the determination of double peaks from increased optical thickness of the Mg II k profile. A large separation of both peaks of 0.3 Å or higher (Jean-Claude Vial, private communication) was used as the main basis to discriminate a profile produced from 2 Doppler components from an optically thick profile. The Mg II k spectra is found to be in general double peaked and broader from increased optical thickness closer to the prominence. On the other hand, the Mg II and Si IV spectra is multiple peaked (with larger Doppler components) and more variable at some distance away from the prominence. For the determination of the non-thermal velocities we took representative temperature formation values for the Mg II k and Si IV 1403 lines of $10,000$ K and $63,000$ K, respectively.

Statistical evolution of the spectral properties during the loop expansion. The behaviour in time of all the spectral properties can be seen in Supplementary Fig. 3. We note a significant variation in the Doppler and non-thermal velocities during the expansion in both the Mg II k and Si IV 1402.77 lines, with an increase of the Doppler velocities mainly towards the blue reaching speeds of 150 km s^{-1}, and a corresponding increase of the non-thermal velocities up to 80 km s^{-1}. The peak and integrated intensities increase up to 2 orders of magnitude above the intensity threshold for detection in Si IV, while in Mg II the profiles have increased integrated intensities and reduced peaks, indicating heating of the initially cool material.

The observed properties of the jets suggest that we can define them based on their dynamics and Si IV intensities. Based on its spectra, we therefore choose to define a jet as an event satisfying both a large enough integrated intensity in the Si IV line (set to twice the average rain emission during the period prior to the loop expansion) and a large enough summed Doppler velocity and non-thermal velocity (where the sum occurs also over all spectral components, and we set this velocity threshold to 100 km s^{-1}). This definition is also supported by our numerical simulation results. We find close to 300 slit pixels satisfying these conditions, all happening during the loop expansion. Supplementary Fig. 3 (bottom panels) shows the histograms of the respective quantities for these pixels, which we define as jet pixels. Although the slit captures the jets at a relatively late stage we can still see that the jets are first highly localised along the loop, and rapidly expand along and down the loop leg (note the very thin peaks in all quantities, each localised within a few arcsecs).

Evolution of braiding and twist of the loop structure. The *IRIS* and *Hinode* observations show several coronal rain strands at high resolution crossing each other near the apex of the loop. At the beginning of the observation there is even some indication of 3 distinct legs spanning from the prominence towards a more or less similar footpoint. It is possible that one of these legs, which is not captured by the IRIS SG slit could actually be only apparently crossing the other 2 due to a LOS superposition effect. We therefore search for the existence of braiding and twist only in the longest lived leg (2 legs disappear leaving only one during most of the observation). The internal misalignment between coronal rain strands can be seen in Supplementary Fig. 4 and amounts to an apparent maximum in the POS of $25^\circ \pm 5^\circ$. The location of the crossing in the POS of strands at the lowest part of the loop (near the apex) seems to coincide with the first location of the microjet occurrence, intensity brightening and plasmoid ejection. Previously red-shifted downflowing plasma is replaced by rapidly evolving blue-shifted strands moving at total speeds of $\approx$ 60 km s^{-1} towards the loop apex. This motion is then replaced by consistently redshifted and blue-shifted strands towards the end of the observation (see last 2 bottom right panels in Supplementary Fig. 4 and the blue/red arrows in Supplementary Fig. 5), respectively at the lowest and highest portions of the loop, suggesting an azimuthal motion (clockwise if observed from apex to right footpoint, as shown in the sketch of Supplementary Fig. 5) of the entire loop structure. An out-of-phase sinusoidal motion of the Mg II intensity in Supplementary Fig. 5 is seen initially between strands, suggesting different internal rotational motion and a complex untwisting motion of the loop. At the same time the loop structure expands, becomes thinner in all spectral channels and the angle between the helical shape of strands and the loop axis is reduced to $10^\circ \pm 3^\circ$. These features suggest an overall reduction in the braiding of a loop from accumulated twist in the structure, which can be appreciated in the time sequence of Supplementary Fig. 4.

EUV light curves and DEM analysis. In order to analyse the evolution of the intensity in the cool and hot channels we average over the loop the SJI 2796, SJI 1400 and AIA 304, AIA 171 and AIA 193 intensities and plot in Supplementary Fig. 6a their normalised values during the time of loop expansion. The SJI 1400 light curve shows 3 bumps, at $t = 84.5$ min, 91 min and 96 min in response to the occurrence of microjets and intensity bursts. It is interesting to note that while AIA 304 shows basically the same evolution as the SJI 1400 channel (suggesting mostly optically thin emission), the second and third intensity bumps are observed in AIA 171 with a 1 minute delay. The AIA 193 also increases steeply as the AIA 171 channel, reaching a maximum at the end of the observation with a continuously increasing trend. This trend from cool to hot emission is also observed in Supplementary Figs. 12-14 (particularly clear when comparing 171, 193 and 211 time-distance maps) for individual cuts across the loop and is clearer towards the footpoint than at the apex (see Supplementary material for details). This trend suggests that the temperature increases first at the apex of the loop and later on towards the footpoint.

The thermal evolution of the coronal plasma can be constrained by the AIA observations. In fact, the observed emission (I_i, in units of $\mathrm{DN}\ s^{-1}\mathrm{pix}^{-1}$) in each AIA narrow EUV passband depends on the thermal properties of the optically thin coronal plasma in the pixel, as follows:

$$I_i = \int_T R_i(T) DEM(T)\, dT \tag{1}$$

where $R_i(T)$ is the response function in the passband i (in units of $\mathrm{DN\ cm^5\ s^{-1}\ pix^{-1}}$), and the differential emission measure (in units of $\mathrm{cm^{-5}K^{-1}}$) is defined by $DEM(T)\, dT = \int_z n_e^2(T)\, dz$, where $n_e^2(T)$ is the electron density of the plasma at temperature T. Here we derive the DEM by applying the inversion method of [31], to the timeseries of the 6 coronal AIA passbands (94, 131, 171, 193, 211, 335). In the plots (e.g., Supplementary Fig. 6b) we show maps of emission measure (EM, in units of $\mathrm{cm^{-5}}$), obtained by integrating the $DEM(T)$ over 0.2 $\log T$ temperature ranges.

The loop can be distinguished in the EM plots of Supplementary Fig. 6b in a wide range of temperatures, from $\log T = 5.5$ (corresponding to the cool EUV material surrounding the condensations), to $\log T = 6.7$ and possibly higher. Despite the possible uncertainties in the determination of the EM, the fact that the pixels along the loop are consistently showing the same temperature range provides support for the presence of these temperatures. We can then confirm temperature maxima of $\log T = 6.3 - 6.5$ and possibly higher.

The observed loop strand in the EUV channel is very thin, with an average thickness of 1400 km. Taking a depth for the structure similar to that in the POS and average EM values of $10^{28} - 10^{28.7}$ cm^{-5} we obtain electron number densities for the EUV emitting material in the range $[8.5 - 19] \times 10^9$ cm^{-3}. The jets, having an average width of 500 km, have number densities in EUV in the range $[1.4 - 3.1] \times 10^{10}$ cm^{-3}. Note that these densities are close but smaller to the densities of the rain strands. It is likely that due to their very small size the jets fail to make a significant deviation to higher EM values. This small difference can also be attributed to the compressibility of the plasma in the reconnection region. The fact that the microjets are mostly absent in the SJI 2796 filter (and Ca II H line for some occurring prior to the loop expansion) also supports a difference in density.

Proposed driver. The observed structure of the loop with small magnetic dips at the apex hosting a prominence is highly reminiscent of the 2.5D MHD numerical model of [22] of what is termed a 'funnel prominence'. In that work a model of a sheared quadrupolar arcade system with an enhanced footpoint heating leads to thermal instability around the apex region where magnetic dips are present. The material slowly accumulates to create a tower-like prominence with coronal rain spilling from the top, displaying very similar dynamics as those observed initially in our observation. In the numerical model, as more material accumulates at the apex the magnetic dips become more pronounced and more stress is placed on the magnetic field. The bending reaches a critical point beyond which magnetic reconnection is triggered, as also predicted by [23], and leads to the formation of a flux rope. The initially bipolar arcade connected to the prominence becomes highly twisted around the flux rope. The authors argue that in a fully 3D model the flux rope would be subject to the kink instability, and therefore could erupt. In this scenario the expansion can be understood as the early stage of the kink instability. This would agree with the bending in the POS of the prominence tower seen in Supplementary Fig. 2a. During the process, reconnection is expected between the highly twisted field lines and the overlying arcade that is still connected to the prominence and coronal rain above. The reconnection process would partially transfer the twist from the flux rope to the loop arcade above, thereby explaining the observed fast internal rotational motions during the expansion.

During the observation, material from the prominence is also observed to fall vertically downwards in Ca II H and Mg II k lines. This feature could indicate slipping of neutral material across the magnetic field below the prominence, as suggested by analytical and observational work [32, 33]. The reduced weight on the field lines above would allow them to expand outwards by magnetic tension. Therefore, this scenario also leads to reconnection between field lines initially connected to the lower part of the prominence with the lowest field lines still connected to the prominence above. In both scenarios the misalignment between the reconnecting field lines in the POS is expected to be small, and the presence of twist would provide the major contribution to the energetics.

The nature of the microjets. The dynamics of the microjets can be understood from component magnetic reconnection between the released (and probably twisted) field lines from below with the field lines at the lowest part of the loop, connected to the prominence above, as sketched in Supplementary Fig. 7. The observed small misalignments in the POS between the rain strands (in the range $10^\circ - 30^\circ$ during the expansion) are then a lower bound to the true misalignment. In this scenario the expected reconnection outflow is partly in the POS, being perpendicular to the rain strands, with a component along the LOS that is determined by the presence of shear and twist. This suggests that the microjet is part of the reconnection outflow and that magnetic tension is the driver of the observed dynamics. However, it is important to note that this kind of microjet is different from the usual reconnection-driven jet concept in the sense that the observed outflow is not directed along the guide field. This is supported by the fact that the ejected plasmoids shown in Fig. 2 are also perpendicular to the loop (being directed along the jet axis), and trace new strands that are rapidly separating downwards from the main loop. The new strands are decelerated and stop at a distance d before disappearing, probably due to heating. Since the observed LOS velocity component of the jets is on the same order as the POS component we should expect a sheared component of the field of the same order as the misalignment in the POS. Numerical work has shown that plasmoids produced by the tearing mode merge in the reconnection exhaust to form larger and slower plasmoids [34]. It is therefore likely that the observed plasmoids are part of the upper tail of the size and energy distribution for such reconnection events.

A curious aspect of the microjets is that, except for a few cases, all point radially inward with respect to the curvature of the loop. Magnetic tension is expected to point mostly inward due to the loop curvature, leading to faster and longer inward jets (and therefore more visible). The strands traced by the plasmoids do in fact exhibit a strong bending (see Fig. 2), supporting magnetic tension as their driving force out of the reconnection region. Also, contrary to the inward jets, the outward jets have the loop as background emission and are therefore much harder to detect. Since all inward jets are mostly blue-shifted we expect the respective outward components to be redshifted. This is supported by the presence of redshifted secondary components for microjet pixels (as seen in Supplementary Figs. 3 and Fig. 15) and the fact that the non-thermal broadening of the jet spectra is of the same order of magnitude as their Doppler shifts.

Energetics. Following the interpretation of the microjets as reconnection outflows and based on the observed characteristics we can estimate the rate of kinetic and thermal energy outflow and compare them with the rate of magnetic energy inflow. We can further estimate the total energy liberated during a single event. Taking a representative total outflow speed of $v_o = 200$ km s^{-1}, inflow densities determined by EUV absorption of $\rho_i = [3.2 \times 10^{10} - 3.2 \times 10^{11}]$ cm^{-3}, outflow densities determined by DEM analysis of $\rho_o = [1.4 - 3.1] \times 10^{10}$ cm^{-3} (keeping in mind that these values are a lower limit), an outflow width ℓ on the same order as the width of the microjet (we take a representative value of $\ell = 500$ km) and an average temperature of 2 MK, we obtain an outflow kinetic energy rate of $[4.7 \times 10^{15} - 1.03 \times 10^{16}]$ erg cm^{-1} s^{-1} and an outflow thermal energy rate of $[5.8 \times 10^{15} - 1.28 \times 10^{16}]$ erg cm^{-1} s^{-1}. Taking a representative time span of 10 s and a representative length of $1,500$ km we estimate the total energy released by a microjet to be $[1 - 2.31] \times 10^{25}$ erg. It is likely that the observed range of energies corresponds to the high end of the distribution of microjets, most of which are expected to occur at lower spatial scales and are unresolved by the present observations.

From previous work we have estimated a magnetic field strength in this loop in the range $B_e = [3.4 - 6.5]$ G, based on the in-situ generation of transverse MHD waves from collision of counter-streaming flows. Taking the POS strand misalignment value as a representative of the angle between the reconnecting strands ($\approx 20°$), we have a shear field component B_N of 1.7 G on average. The inflow electromagnetic energy into the reconnection region is given by the Poynting flux and using the conservation of mass it becomes $v_o \ell \frac{B_N^2}{4\pi} = 2.3 \times 10^{14}$ erg cm^{-1} s^{-1}, where we assume an outflow density equal to the inflow density. It is also likely that the value of the magnetic field during the expansion increases due to the addition of the field below, producing the reconnection. If we require that the inflowing magnetic energy has the same magnitude as the outflowing kinetic and thermal energies then the required field strengths are $22-37$ G.

Numerical modelling of microjets. In order to better understand the dynamics of the microjets generation in the solar corona, we devise non-ideal MHD simulations where two adjacent and parallel, gravitationally stratified coronal loops are slightly tilted, in accordance with the observed small POS crossings between rain strands prior to the microjets.

The setup we use here is inspired from [35, 36]. We consider a 3D cartesian reference frame where x and y are the directions perpendicular to the loops axes and z is the direction along the loop axes. The initial configuration is constructed by considering a gravitationally stratified solar atmosphere where we have a chromosphere-like layer where the density is followed by a transition region and a million degree corona. Two flux tubes representative of coronal loops are defined by a stronger magnetic field (between $x=-2.2$ Mm and $x=2.2$ Mm and around $y=0$) and are allowed to relax by numerically solving the 3D resistive MHD equations with the PLUTO code [37]. The MHD equations include thermal conduction and radiative losses, and incorporate an anomalous magnetic resistivity term that switches on to (otherwise) non-zero values whenever the current density exceeds a specific threshold. The details of the MHD equations can be found in the Supplementary Information.

The numerical domain extends over 48.7 Mm in the horizontal direction (x and y directions) with a non-uniform grid and the highest resolution is achieved in the central 20 Mm part of the domain, where the grid cell size is 60 km. In the vertical direction (z) the domain is 62 Mm long and we have 128 points distributed along a stretched grid in the coronal part of the domain. We impose closed boundary conditions in x and y and reflective at z boundaries, which are far enough to not influence the evolution of the two central flux tubes under attention here.

We impose a transient driver at the chromospheric footpoints of both loops that slowly drifts them apart, in opposite directions in such a way as to generate a slight x-type misalignment in the corona. The response of the magnetic field in the corona lags with respect to the evolution of the chromospheric footpoints, as signals need to propagate through the chromosphere and transition region. Only at $t = 180$ s (the end of the driving phase) a significant V_y component of the plasma speed appears in the corona (see Supplementary Fig. 8a). At the same time, such dynamics trigger the oscillation of the coronal magnetic field before it relaxes towards a new equilibrium prescribed by the tilted configuration.

Given the geometry of the system, the tilt angle θ_t between both footpoints is defined as

$$\theta_t = \sin^{-1}\left(\frac{B_y}{|B|}\right), \tag{2}$$

where we consider the average B_y and $|B|$ along the loop. The rearrangement of the magnetic field in the solar corona leads to a steady increase of the misalignment angle θ_t between both loops, from 3° at $t \approx 180$ s to almost 8° at $t \approx 360$ s (Supplementary Fig. 8b), before slightly decreasing.

An increase of the tilt angle of the two loops implies an increase of the electric current in between (Supplementary Fig. 9a). Near the time $t = 380$ s, the electric current between the loops overcomes the threshold for the anomalous resistivity and the magnetic field diffusion sets in. At this time, the characteristic length L of the region in which the electric currents are larger than the threshold is about 0.3 Mm, the plasma velocity V is of the order of 50 km s^{-1}, and the resistivity coefficient is $\eta_0 = 10^{14}$ cm^{-2} s^{-1}. This leads to a magnetic Reynolds number of

$$R_M = \frac{VL}{\eta_0} \sim 1. \tag{3}$$

In this regime the time scales for the diffusion and advection of the magnetic field are similar and we expect non-ideal effects, and in particular the onset of magnetic reconnection.

As soon as magnetic reconnection sets in, magnetic field lines change connectivity from one loop to the other, with a change of direction (the module of the B_y component of the magnetic field grows up to 0.07 G before flipping sign after the reconnection) at the centre of the domain. This changed topology leads to an enhanced magnetic tension in that region (Supplementary Fig. 9b), which starts displacing the plasma transversely. Accordingly, the velocity V_y of the plasma rapidly increases (Supplementary Fig. 9c) to well above 200 km s^{-1}, which is much higher than any plasma velocity previously found in the simulation.

Focusing in a volume near the centre of the domain, we find that the magnetic energy initially increases with the y-component of the local magnetic field (see Supplementary Fig. 8b). When the anomalous resistivity is triggered and the diffusion of the magnetic field occurs, the magnetic energy drops to a value lower than the initial one. This magnetic energy decrease coincides with an increase of the thermal and kinetic energy that occurs on a very similar timescale and magnitude of energy jump (Supplementary Fig. 10a). The kinetic energy increase appears smaller because is more localised and because part of the kinetic energy is quickly converted into thermal energy during the plasma compression. Such kinetic energy increase is associated with an average speed of $\sim$ 140 km s^{-1}, whereas the plasma is accelerated locally up to $\sim$ 300 km s^{-1}. We identify as jets the localised regions near the centre of the domain where the plasma is accelerated to hundreds of km/s (see Fig. 5f). The temperature increases already when the loops are being tilted, but increases faster when the reconnection is triggered (Supplementary Fig. 10b). This second temperature jump is of the order of 3×10^6 K. In Supplementary Fig. 10c we show an estimation of the electromagnetic inflow rate computed as:

$$F_m = \frac{v_{out} B_N^2 \ell}{4\pi} \tag{4}$$

where v_{out} is the outflow velocity where the jet develops, that we estimate from the maximum $y-$component of the velocity along the axis $x = 0$ $z = 0$, B_N is the magnetic field inflow component that we compute from the average $y-$component of the magnetic field in one loop at $z = 0$, and ℓ is the spatial scale on which the reconnection occurs that we estimate visually as $\ell = 1.3$ Mm (width of the box in Fig. 5f). The maximum value of F_m is attained for $v_{out} \approx$ 260 km s^{-1} and $B_N = 1.9$ G. We find that the outflow thermal energy rate ($\frac{3}{2} n k_B T v_o \ell$) is comparable to the inflow electromagnetic energy rate. On the other hand, the outflow kinetic energy rate ($\frac{1}{2} \rho v_o^3 \ell$) is much smaller because of the localisation of the velocities.

Fig. 5 summarises the 3D configuration of the system when magnetic reconnection occurs and illustrates the jet geometry and dynamics. The region where the electric current is equal to the threshold to trigger the anomalous resistivity has an X-shape and is located between the two loops (Figs. 5a and 5d). The highest velocities are highly localised around the centre of the domain (Fig. 5e), where the region with $|V_y| \geq 190$ km s^{-1} is a few Mm long. However, high V_y velocities around or above 100 km s^{-1} are also found along the reconnected field lines to a distance half-way down the loop (Fig. 5b), indicating a strong transverse motion of the entire reconnecting strand. Importantly, the high velocity region at the centre is adjacent to the reconnected magnetic field lines (black lines) that show near $z = 0$ a curvature generating an outward magnetic tension, as diagnosed in Supplementary Fig. 9. Such configuration is not found at earlier stages of the simulation before the magnetic field is allowed to reconnect. We also find that the longitudinal velocities (V_z) are always on the order of a few tens of km s^{-1} or less (Fig. 5c). Hence, in this model the reconnection triggers the highest velocities mostly along the y-direction, i.e. perpendicular to the guide magnetic field and coronal loop axes, and only minor motions along the loops.

The considered numerical model leads to results with the same telltale signatures as those of the observed microjets. We have very similar dynamics (strong transverse motion of strands, with localised very fast transverse jet-like motion adjacent to the reconnected strands), geometry (small misalignments between strands, highly localised perpendicular bursts around the reconnection region) and temperature increase (at the reconnection region and along the loop). The changes occur in a timescale of 100 s, which is longer than the observed timescale of a single microjet (10 s or less) but similar to that of the microjet clusters. Also, the localisation of the jets in the numerical model is roughly 5 times larger than that of a single microjet in the observations, but similar to the width of the microjet cluster. Although our model does not capture the exact conditions of the observed plasma (partially ionised, cool and dense), we consider that the same physics would occur in more detailed experiments. The differences with the numerical experiment, in particular, the single and clustered occurrences of the microjets at faster timescales and smaller length scales, accompanied by plasmoids, constitute a challenge for future numerical models of magnetic reconnection that can clarify the detailed physics of this process in the solar corona.

1. Klimchuk, J. A. Key aspects of coronal heating. *Philosophical Transactions of the Royal Society of London Series A* **373**, 20140256–20140256 (2015). `1410.5660`.

2. Biskamp, D. Magnetic reconnection via current sheets. *The Physics of Fluids* **29**, 1520–1531 (1986). URL `https://aip.scitation.org/doi/abs/10.1063/1.865670`. `https://aip.scitation.org/doi/pdf/10.1063/1.865670`.

3. Zweibel, E. G. & Yamada, M. Magnetic reconnection in astrophysical and laboratory plasmas. *Annual Review of Astronomy and Astrophysics* **47**, 291–332 (2009). URL `https://doi.org/10.1146/annurev-astro-082708-101726`. `https://doi.org/10.1146/annurev-astro-082708-101726`.

4. Bhattacharjee, A., Huang, Y.-M., Yang, H. & Rogers, B. Fast reconnection in high-lundquist-number plasmas due to the plasmoid instability. *Physics of Plasmas* **16**, 112102 (2009). URL `https://doi.org/10.1063/1.3264103`. `https://doi.org/10.1063/1.3264103`.

5. Takasao, S., Asai, A., Isobe, H. & Shibata, K. Simultaneous Observation of Reconnection

Inflow and Outflow Associated with the 2010 August 18 Solar Flare. *ApJL* **745**, L6 (2012). `1112.1398`.

6. Reale, F., Peres, G., Serio, S., DeLuca, E. E. & Golub, L. A Brightening Coronal Loop Observed by TRACE. I. Morphology and Evolution. *ApJ* **535**, 412–422 (2000).
7. Reale, F. *et al.* A Brightening Coronal Loop Observed by TRACE. II. Loop Modeling and Constraints on Heating. *ApJ* **535**, 423–437 (2000).
8. Rouppe van der Voort, L. *et al.* Intermittent Reconnection and Plasmoids in UV Bursts in the Low Solar Atmosphere. *ApJL* **851**, L6 (2017). `1711.04581`.
9. Li, L. *et al.* Magnetic reconnection between a solar filament and nearby coronal loops. *Nature Physics* **12**, 847 EP – (2016). URL `https://doi.org/10.1038/nphys3768`.
10. Reeves, K. K., McCauley, P. I. & Tian, H. DIRECT OBSERVATIONS OF MAGNETIC RECONNECTION OUTFLOW AND CME TRIGGERING IN a SMALL ERUPTING SOLAR PROMINENCE. *The Astrophysical Journal* **807**, 7 (2015). URL `https://doi.org/10.10882F0004-637x2F8072F12F7`.
11. Parker, E. N. Nanoflares and the solar X-ray corona. *ApJ* **330**, 474–479 (1988).
12. Cargill, P. J. Some implications of the nanoflare concept. *ApJ* **422**, 381–393 (1994).
13. Rappazzo, A. F., Velli, M., Einaudi, G. & Dahlburg, R. B. Nonlinear Dynamics of the Parker Scenario for Coronal Heating. *ApJ* **677**, 1348–1366 (2008). `0709.3687`.

14. Ishikawa, S. *et al.* Detection of nanoflare-heated plasma in the solar corona by the foxsi-2 sounding rocket. *Nature Astronomy* **1**, 771–774 (2017).

15. Moriyasu, S., Kudoh, T., Yokoyama, T. & Shibata, K. The Nonlinear Alfvén Wave Model for Solar Coronal Heating and Nanoflares. *ApJL* **601**, L107–L110 (2004).

16. Antolin, P., Shibata, K., Kudoh, T., Shiota, D. & Brooks, D. Predicting Observational Signatures of Coronal Heating by Alfvén Waves and Nanoflares. *ApJ* **688**, 669–682 (2008).

17. Lu, E. T., Hamilton, R. J., McTiernan, J. M. & Bromund, K. R. Solar flares and avalanches in driven dissipative systems. *ApJ* **412**, 841–852 (1993).

18. Charbonneau, P., McIntosh, S. W., Liu, H.-L. & Bogdan, T. J. Avalanche models for solar flares (Invited Review). *Sol.Phys.* **203**, 321–353 (2001).

19. Aschwanden, M. J. *et al.* 25 Years of Self-Organized Criticality: Solar and Astrophysics. *SSRv* **198**, 47–166 (2016). `1403.6528`.

20. Hood, A. W., Cargill, P. J., Browning, P. K. & Tam, K. V. AN MHD AVALANCHE IN a MULTI-THREADED CORONAL LOOP. *The Astrophysical Journal* **817**, 5 (2016). URL `https://doi.org/10.3847/0004-637X/817/1/5/meta`.

21. De Pontieu, B. *et al.* The Interface Region Imaging Spectrograph (IRIS). *Sol.Phys.* **289**, 2733–2779 (2014). `1401.2491`.

22. Keppens, R. & Xia, C. The Dynamics of Funnel Prominences. *ApJ* **789**, 22 (2014). `1405.3419`.

23. Low, B. C., Liu, W., Berger, T. & Casini, R. The Hydromagnetic Interior of a Solar Quiescent Prominence. II. Magnetic Discontinuities and Cross-field Mass Transport. *ApJ* **757**, 21 (2012).

24. Antolin, P. & Rouppe van der Voort, L. Observing the Fine Structure of Loops through High-resolution Spectroscopic Observations of Coronal Rain with the CRISP Instrument at the Swedish Solar Telescope. *ApJ* **745**, 152 (2012). `1112.0656`.

25. Antolin, P., Pagano, P., De Moortel, I. & Nakariakov, V. M. In Situ Generation of Transverse Magnetohydrodynamic Waves from Colliding Flows in the Solar Corona. *ApJL* **861**, L15 (2018). `1807.00395`.

26. Suematsu, Y. *et al.* The Solar Optical Telescope of Solar-B (Hinode): The Optical Telescope Assembly. *Sol.Phys.* **249**, 197–220 (2008).

27. Tsuneta, S. *et al.* The Solar Optical Telescope for the Hinode Mission: An Overview. *Sol.Phys.* **249**, 167–196 (2008). `0711.1715`.

28. Lemen, J. R. *et al.* The Atmospheric Imaging Assembly (AIA) on the Solar Dynamics Observatory (SDO). *Sol.Phys.* **275**, 17–40 (2012).

29. Antolin, P., Vissers, G., Pereira, T. M. D., Rouppe van der Voort, L. & Scullion, E. The Multithermal and Multi-stranded Nature of Coronal Rain. *ApJ* **806**, 81 (2015). `1504.04418`.

30. Landi, E. & Reale, F. Prominence Plasma Diagnostics through Extreme-ultraviolet Absorption. *ApJ* **772**, 71 (2013). `1209.2934`.

31. Cheung, M. C. M. *et al.* Thermal Diagnostics with the Atmospheric Imaging Assembly on

board the Solar Dynamics Observatory: A Validated Method for Differential Emission Measure Inversions. *ApJ* **807**, 143 (2015). `1504.03258`.

32. Gilbert, H. R., Hansteen, V. H. & Holzer, T. E. Neutral Atom Diffusion in a Partially Ionized Prominence Plasma. *ApJ* **577**, 464–474 (2002).
33. Gilbert, H., Kilper, G. & Alexander, D. Observational evidence supporting cross-field diffusion of neutral material in solar filaments. *The Astrophysical Journal* **671**, 978 (2007). URL `http://stacks.iop.org/0004-637X/671/i=1/a=978`.
34. Huang, Y.-M. & Bhattacharjee, A. Distribution of plasmoids in high-lundquist-number magnetic reconnection. *Phys. Rev. Lett.* **109**, 265002 (2012). URL `https://link.aps.org/doi/10.1103/PhysRevLett.109.265002`.
35. Petralia, A., Reale, F., Orlando, S. & Testa, P. Bright Hot Impacts by Erupted Fragments Falling Back on the Sun: Magnetic Channelling. *ApJ* **832**, 2 (2016). `1609.04634`.
36. Petralia, A., Reale, F. & Testa, P. Guided flows in coronal magnetic flux tubes. *A&A* **609**, A18 (2018). `1711.04641`.
37. Mignone, A. *et al.* The PLUTO Code for Adaptive Mesh Computations in Astrophysical Fluid Dynamics. *ApJS* **198**, 7 (2012). `1110.0740`.
38. Anders, E. & Grevesse, N. Abundances of the elements - Meteoritic and solar. *GCA* **53**, 197–214 (1989).
39. Spitzer, L. *Physics of Fully Ionized Gases* (Interscience Publishers, 1962).

40. Alexiades, V., Amiez, G. & Gremaud, P.-A. Super-time-stepping acceleration of explicit schemes for parabolic problems. *Communications in Numerical Methods in Engineering* **12**, 31–42 (1996).

41. Landi, E., Del Zanna, G., Young, P. R., Dere, K. P. & Mason, H. E. CHIANTI - An Atomic Database for Emission Lines. XII. Version 7 of the Database. *ApJ* **744**, 99 (2012).

42. Dere, K. P. *et al.* CHIANTI - an atomic database for emission lines. IX. Ionization rates, recombination rates, ionization equilibria for the elements hydrogen through zinc and updated atomic data. *A&A* **498**, 915–929 (2009).

43. Linker, J. A., Lionello, R., Mikić, Z. & Amari, T. Magnetohydrodynamic modeling of prominence formation within a helmet streamer. *JGR* **106**, 25165–25176 (2001).

44. Lionello, R., Linker, J. A. & Mikić, Z. Multispectral Emission of the Sun During the First Whole Sun Month: Magnetohydrodynamic Simulations. *ApJ* **690**, 902–912 (2009).

45. Mikić, Z., Lionello, R., Mok, Y., Linker, J. A. & Winebarger, A. R. The Importance of Geometric Effects in Coronal Loop Models. *ApJ* **773**, 94 (2013).

46. Johnston, C. D. & Bradshaw, S. J. A Fast and Accurate Method to Capture the Solar Corona/Transition Region Enthalpy Exchange. *ApJL* **873**, L22 (2019). `1903.01132`.

47. Balsara, D. S. & Spicer, D. S. A Staggered Mesh Algorithm Using High Order Godunov Fluxes to Ensure Solenoidal Magnetic Fields in Magnetohydrodynamic Simulations. *Journal of Computational Physics* **149**, 270–292 (1999).

48. Serio, S., Peres, G., Vaiana, G. S., Golub, L. & Rosner, R. Closed coronal structures. II - Generalized hydrostatic model. *ApJ* **243**, 288–300 (1981).

49. Guarrasi, M., Reale, F., Orlando, S., Mignone, A. & Klimchuk, J. A. MHD modeling of coronal loops: the transition region throat. *A&A* **564**, A48 (2014). `1402.0338`.

Acknowledgements P.A. acknowledges funding from his STFC Ernest Rutherford Fellowship (No. ST/R004285/1) and support from the International Space Science Institute, Bern, Switzerland to the International Teams on 'Implications for coronal heating and magnetic fields from coronal rain observations and modeling' and 'Observed Multi-Scale Variability of Coronal Loops as a Probe of Coronal Heating'. This project has received funding from the European Research Council (ERC) under the European Union's Horizon 2020 research and innovation programme (grant agreement No 647214). P.T. acknowledges support by 8100002705 and SP02H1701R from Lockheed-Martin to SAO. *Hinode* is a Japanese mission developed and launched by ISAS/JAXA, with NAOJ as domestic partner and NASA and STFC (UK) as international partners. It is operated by these agencies in co-operation with ESA and NSC (Norway). *IRIS* is a NASA small explorer mission developed and operated by LMSAL with mission operations executed at NASA Ames Research Center and major contributions to downlink communications funded by ESA and the Norwegian Space Centre. *SDO* is part of NASA's Living With a Star Program. This work used the DiRAC Data Centric system at Durham University, operated by the Institute for Computational Cosmology on behalf of the STFC DiRAC HPC Facility. This equipment was funded by a BIS National E-infrastructure capital grant ST/K00042X/1, STFC capital grant ST/K00087X/1, DiRAC Operations grant ST/K003267/1, and Durham University. DiRAC is part of the National E-Infrastructure. We acknowledge the use of the open source (gitorious.org/amrvac) MPI-AMRVAC software.

Author contributions statement P.A. was responsible for the planning, coordination, image processing, analysis of the observations and redaction of most of the manuscript. P.P. was responsible for the numerical simulations and redacted the analysis of the numerical results. P.T. was responsible for the differential emission measure analysis and redacted the corresponding section in the manuscript. A.P. and F.R. have provided the numerical code and the initial condition to the numerical simulation. A.P., F.R. and P.T. have also provided feedback on the analysis of the results and the redaction of the manuscript.

Supplementary material

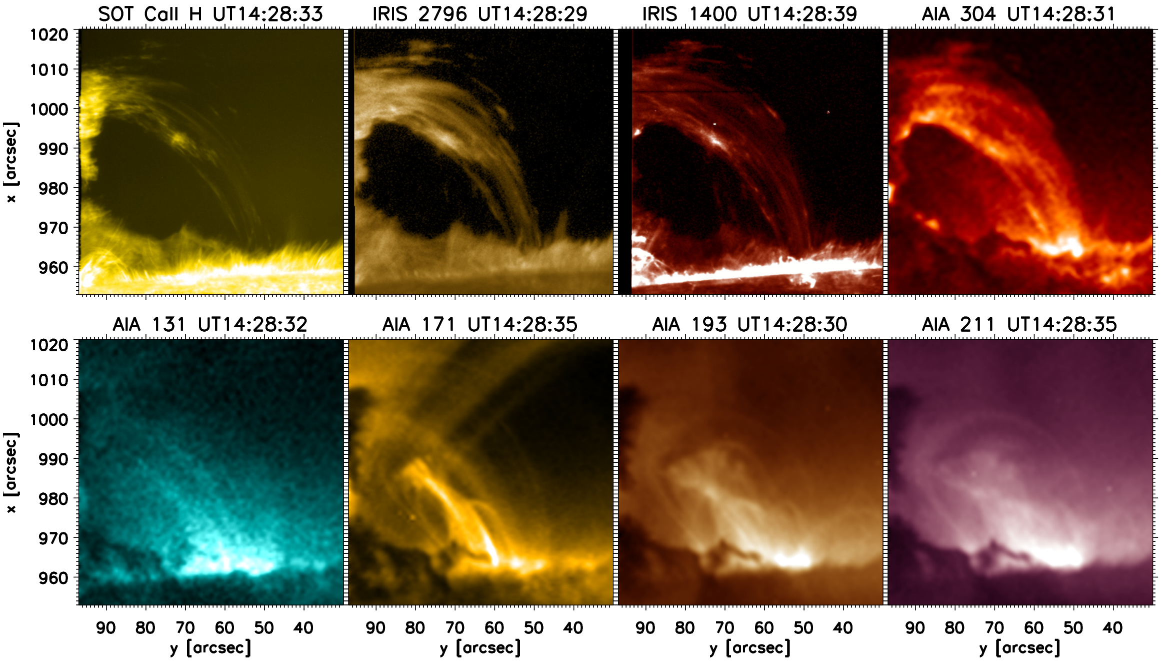

Supplementary Figure 1: **Common FOV to *Hinode*/SOT, *IRIS* and *SDO*/AIA.** From top left to bottom right we show in order of increasing temperature formation, the common FOV of the coordinated observation at the same time shown in Fig. 1. Chromospheric temperatures are represented by the SOT Ca II H and SJI 2796 channels ($\log T \approx 4-4.2$). Lower transition region temperatures are represented by SJI 1400 and AIA 304 ($\log T \approx 4.8-5$). Upper transition region temperatures are represented by AIA 131 and 171 ($\log T \approx 5.7-5.9$). Coronal temperatures are best observed by AIA 193 and 211 ($\log T \approx 6.2-6.3$). A radial filter has been applied to the SOT, *IRIS* 2796 and *IRIS* 1400 images to decrease the disk intensity and to make the off-limb features more visible. An animation of this figure is available online.

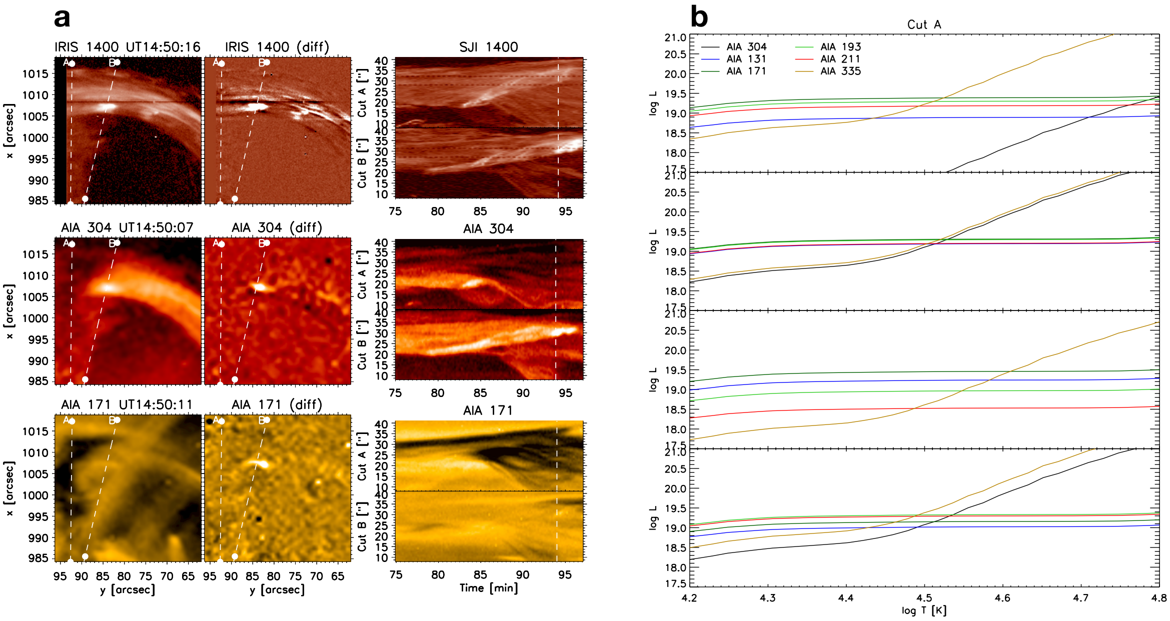

Supplementary Figure 2: **Dynamics of the prominence core.** Panels **a**: From top to bottom the panels show a pair of a snapshot and its running difference version of a $34'' \times 34''$ portion at the apex of the loop in the *IRIS* 1400, AIA 304 and AIA 171 channels, respectively, closest in time to the AIA 304 image. The panels on the right to each image pair shows the time-distance image along cuts A and B (white dashed lines in the images) for the last 24 min of observation and for a distance corresponding to that between the white filled circles along each cut. The moment in time of the images is indicated by the white vertical dashed line in the time-distance image. The cool prominence material produces dark EUV absorption features in the 171 channel. Many filamentary threads are seen going downwards towards the solar surface. An animation for panels **a** is available online. Panels **b**: We select 4 of the isolated prominence threads going downwards and calculate the $L(T)$ function for each thread and channel (see text for details). The location of intersection of all L functions indicate a common temperature at a specific hydrogen column density.

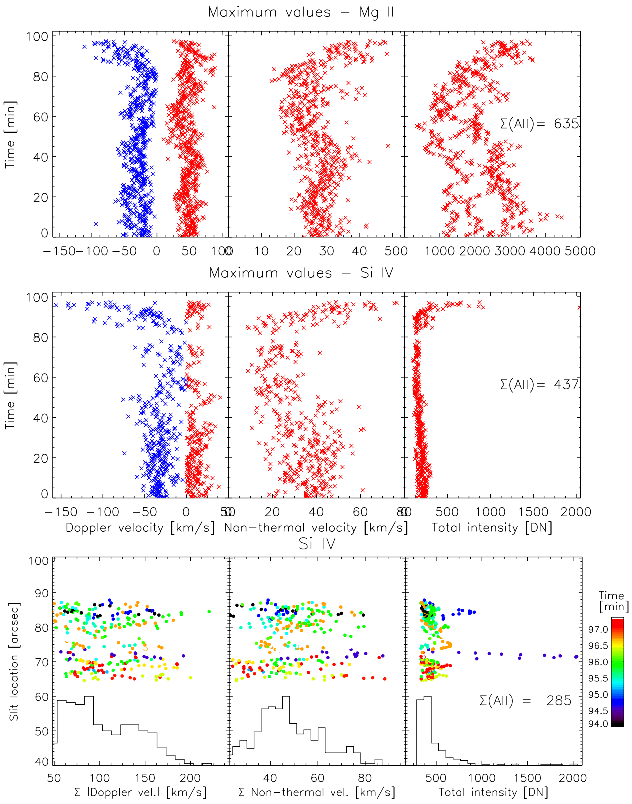

Supplementary Figure 3: **Evolution of the rain spectral components and statistics of jets**. For each time step we show the maximum of the measured spectral quantity (Doppler velocity, non-thermal velocity or integrated intensity) for the Mg II k (top panels) and Si IV 1402.77 (middle panels) lines along the slit and among all spectral components for each slit pixel (including main components and residuals). In the Doppler velocity plot the maxima are taken separately between blue- (shown in blue) and redshifted values (shown in red). The integrated intensity is calculated over the entire line profile (above background noise). The slit pixels corresponding to microjets are chosen (bottom panels) based on the total intensity and the total velocity (see text for details). The time evolution is shown with different colours. Histograms for each quantity are shown at the bottom of each plot. Note that the microjets are characterised by increases in intensity, Doppler velocity and non-thermal velocity that are very localised in time.

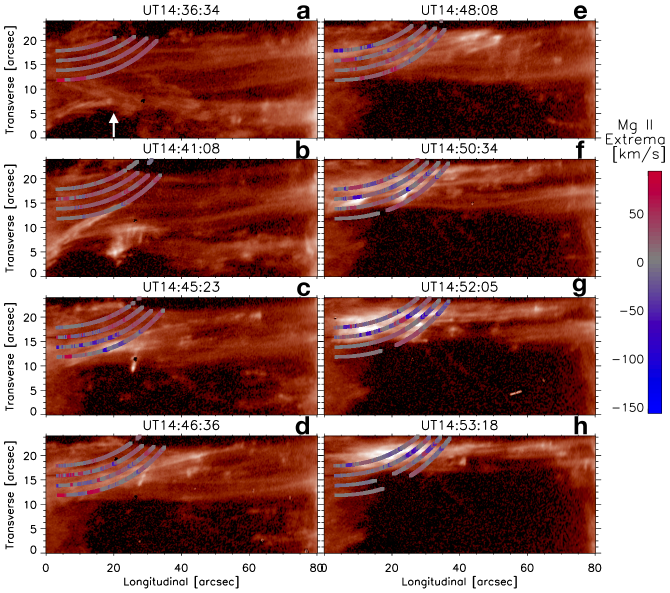

Supplementary Figure 4: **Evolution of twist along the loop.** A slab containing the loop is selected and we interpolate the slab into a rectangle in order to eliminate the loop curvature and better observe the presence of twist (x and y scales are different in the image). We select several snapshots towards the end of the observation and overlay the Doppler velocity (extrema among the multiple components at each pixel) measured from the *IRIS* slit. The evolution goes from **a** to **h** panels. Panel **a** shows the state of the loop just prior to the loop expansion. Note the presence of braiding. Particularly, 2 rain strands can be seen intersecting each other (white arrow in panel). Minutes later, panel **b** shows that one of the 2 intersecting strands has brightened and moved rapidly outward (and is blueshifted, contrary to the rest of the loop), while the other strand exhibits the clustered appearance of microjets and plasmoid ejections. The following snapshots **(c to h)** indicate the rapid outward motion of the strands, local brightening events and the gradual reduction of twist along the loop. During this motion the strands at the lower part of the loop are on average redshifted while the upper part of the loop is blueshifted, suggesting an untwisting motion sketched in Supplementary Fig. 5. An animation of this figure is available online.

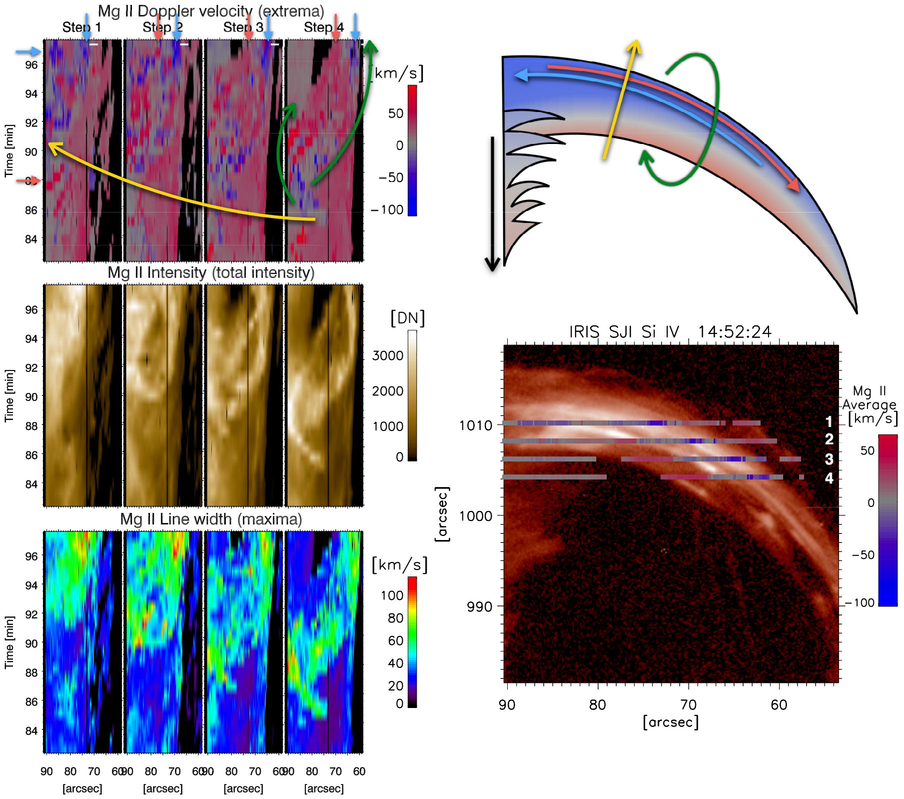

Supplementary Figure 5: **Time-distance maps of spectral features during the loop expansion.** Left column: From top to bottom we display the time-distance maps of Mg II k Doppler velocity, total (integrated) intensity and line width along the slit for each raster position, where the raster step number is assigned as indicated in the right image (corresponding to SJI 1400). The Doppler velocity and line width values correspond, respectively, to the extrema and maxima among all spectral components for each pixel. The intensities correspond to the integrated intensities over the Mg II k profile (with sufficient SNR). The red/blue pairs of arrows and the green curved arrows in the Doppler maps (and in the sketch) highlight a motion suggestive of rotation. Top right panel: Sketch of the average motion observed along the loop towards the end of the observation. The yellow arrow (also in the Doppler map) indicates the progression of the expansion. The location in time of the SJI 1400 image on the bottom right is indicated by the small white mark in each raster.

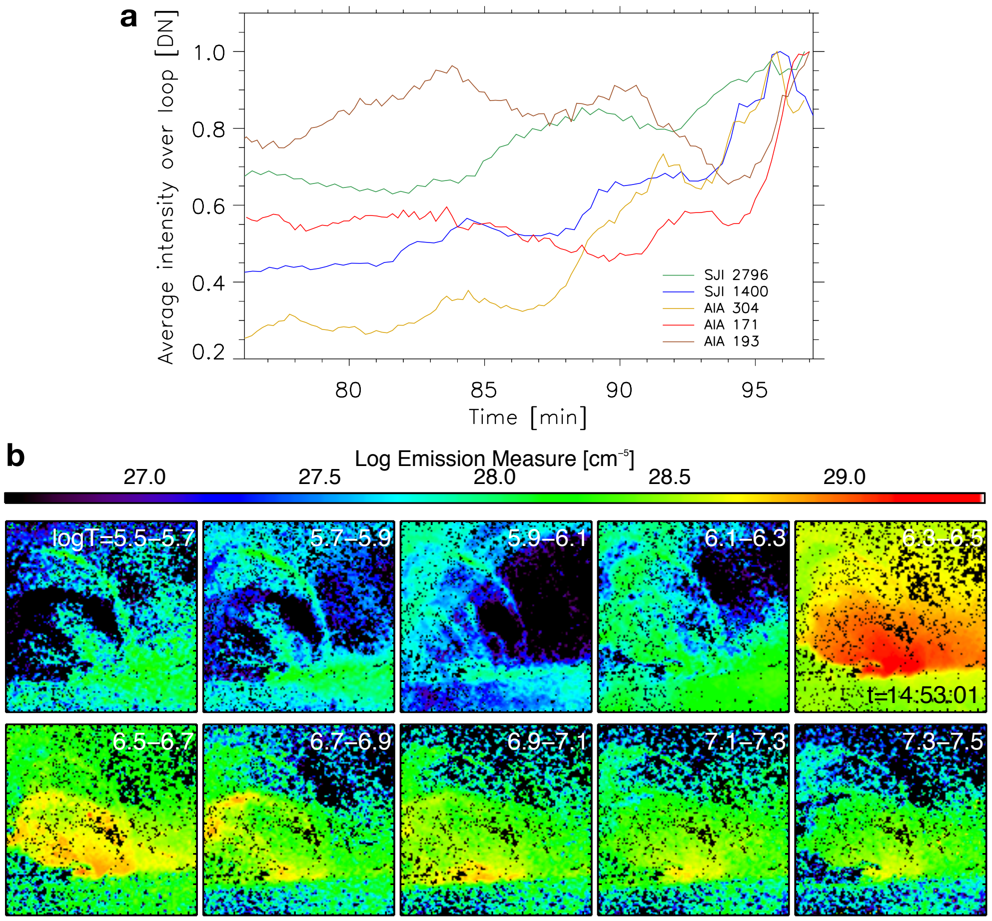

Supplementary Figure 6: **EUV lightcurves and emission measure.** We select a curved slab containing the loop of interest (and avoiding most bright structures along the LOS present in the hot channels), average the intensity in the entire slab for the SJI channels and AIA 304, 171 and 193 channels and plot this quantity normalised to its maximum over the last 22 min of observation (panel **a**). See the legend in the figure for the colour corresponding to each channel. For the DEM analysis (panels **b**) the temperature range is binned in intervals of $\log T = 0.2$ and the emission measure of the region of interest for each bin is displayed. The FOV is the same as in Supplementary Fig. 1. Note the presence of hot plasma along the loop at temperatures of $\log T = 6.3 - 6.5$ (and possibly at higher temperatures as well). An animation corresponding to the bottom panels is available online.

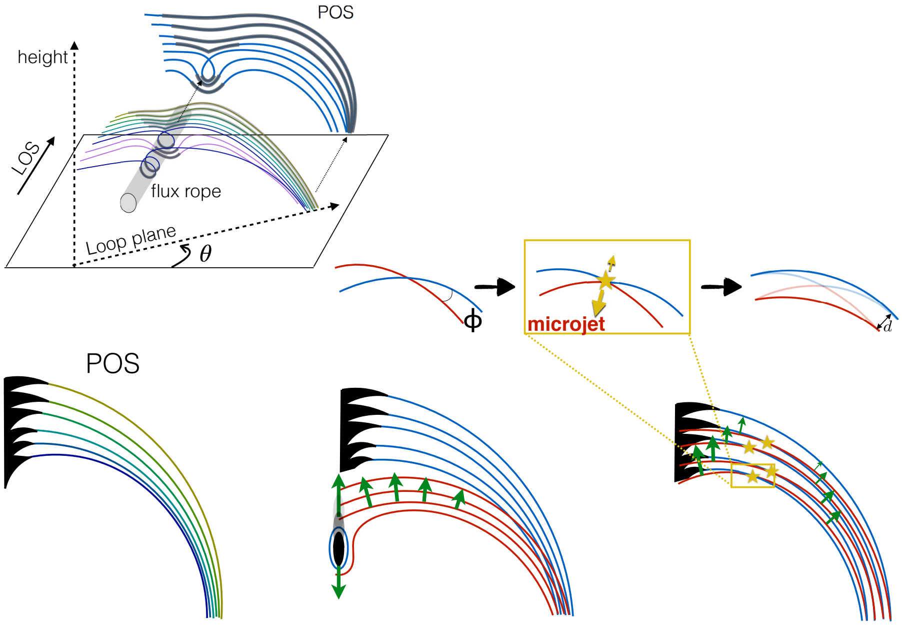

Supplementary Figure 7: **Sketch of the observed structure and interpretation of the microjet driver.** The top sketch shows a 3D view of the observed structure at the end of the observation. The loop plane makes an angle θ with respect to the POS plane. The flux rope formed by reconnection and coronal rain material is indicated in grey colour. Field lines (shown in different colours) below the loop are twisted around the prominence material (thus forming the flux rope). The 3 sketches on the bottom indicate the POS view, where the prominence material is shown in black. At a late stage, part of the prominence material falls downward as indicated in the bottom-middle sketch, releasing magnetic field lines through reconnection or neutral material slipping through field lines. The (twisted) magnetic field lines (in red) move up by magnetic tension and the entire structure starts to expand. The released magnetic field lines push the upper field lines still anchored to the prominence above forming small misalignments (angle ϕ) and driving component magnetic reconnection between the red and blue field lines. The microjets result from this reconnection process. The reconnected field lines find a new equilibrium, separated by a distance d.